Acoustic scattering comparison of Kirchhoff approximation to Rayleigh-Fourier method for sinusoidal surface waves at low grazing angles

Edward L. Richards,[a] H. C. Song, and W. S. Hodgkiss
Scripps Institution of Oceanography, La Jolla, California 92093, USA

The Fourier series method for implementing the Rayleigh hypothesis [Rayleigh-Fourier method (RFM)] is used as a reference solution to assess the Kirchhoff approximation of the Helmholtz integral [Helmholtz-Kirchhoff approximation (HKA)] for modeling broadband scatter from sinusoidal surfaces at low grazing angles. The HKA is a valuable solution because it has an eigen-ray interpretation without unbounded caustic amplitudes and discontinuous shadow zones. Plane wave studies of the HKA, however, show it becomes inaccurate at low grazing angles. This study quantifies how this limitation manifests with increasing transmission distance for time domain scattering simulations. Scattering results are compared over a complete surface wave cycle with parameters modeling sea surface-swell. The HKA agrees reasonably well with the RFM in point source calculations for limited extensions of transmission distances beyond where plane wave comparisons begin to diverge. Past these distances, HKA solutions begin to show significant over-prediction of the acoustic amplitude around late arrivals. This over-prediction is frequency dependent and eigen-ray interference offers an explanation of this behavior. Further extending the transmission range leads to a significant HKA error, and a range is found at which flat surface reflections have less error.
© 2018 Acoustical Society of America. https://doi.org/10.1121/1.5052256

[BTH]   Pages: 1269–1278

I. INTRODUCTION

Modeling time-domain acoustic scatter from deterministic, two-dimensional sea surfaces remains a computationally challenging task and practicality requires approximate methods of solution. The Helmholtz-Kirchhoff approximation (HKA) is often used for scattering calculations from general sea surfaces. It is straightforward to calculate and offers an interpretation of the solution through its eigen-ray approximation (ERA). This study seeks to establish experimental geometries where the HKA may be expected to give reasonable scattering results by comparing it to a reference Rayleigh-Fourier method (RFM). The RFM requires periodic scattering surfaces, and a sinusoidal surface is used for comparison. By establishing experimental geometries where the HKA is accurate for a simplified surface, this comparison lends credence to the approximation for surfaces without a simple reference solution.

A. HKA

A number of approximate surface scattering solutions exist in underwater acoustics literature, including the small slope approximation (Thorsos and Broschat, 1995), the parabolic equation (i.e., Senne *et al.*, 2012), the wedge assemblage method (Keiffer and Novarini, 2000), and the Kirchhoff approximation of the Helmholtz integral (HKA) (Meecham, 1956). The HKA recently has been used for wave tank studies: as a forward model in an inverse method

determining the shape of the surface wave (Walstead and Deane, 2013), and to create scattering statistics (Walstead and Deane, 2016). Additionally, the HKA has been used for three-dimensional (Choo *et al.*, 2016) and refractive environment (Choo *et al.*, 2017) time domain scatter modeling.

The time domain form of the HKA is an extension of eigen-ray theory, building scattered time series with scaled and delayed transmissions from a number of surface interactions. The delay of each of the interactions, or rays, is the sum of the acoustic travel time to the surface point from the source and receiver. Whereas eigen-ray solutions only include contributions from rays which reflect specularly, the HKA includes rays from every point along the surface. The stationary phase approximation may be used to produce the ERA from the HKA surface integral, and each stationary point in travel time along the surface corresponding to an eigen-ray (Williams *et al.*, 1994).

The ERA of the HKA integral breaks down when it cannot be described with first-order stationary phase approximations. The most common breakdown of the ERA occurs in caustic regions where two eigen-rays coincide. To avoid inaccuracies introduced by the ERA this study uses numerical quadrature to solve the HKA, although higher-order stationary phase approximations provide similar results (Williams *et al.*, 1994). The ERA is found to be a good approximation of the HKA only short distances away from where it breaks down, however. Once the HKA result is used to find locations of interest, the ERA may be used to explain frequency-dependent focusing observed in the HKA at ranges where HKA begins to show significant error.

a)Electronic mail: edwardlrichards@ucsd.edu

Describing the HKA as a superposition of rays can also explain the shortcomings of the approximation. Plane wave studies (e.g., Thorsos, 1988) have shown that the HKA becomes significantly inaccurate at lower grazing angles. This inaccuracy at low grazing angles is attributed to the inability of the HKA to model how one part of the surface interacts with the acoustic field at another part of the surface (Liszka and McCoy, 1982). Shadowing effects, which occur when one portion of the surface blocks straight line propagation to another part of the surface, are simple to understand and test. However this study will not use shadowing corrections to the HKA because straightforward implementations did not yield any marked improvements of the results.

Meecham (1956) used the Helmholtz integral equation (HIE) to study the surface self-interaction not modeled in the HKA. The HIE is a solution to the Helmholtz equation and surface boundary condition, using both the HKA and an additional integral of the unknown pressure field at the scattering surface. This unknown pressure field may be found with an iterative method that uses the HKA as an initial guess. With a stationary phase approximation of this iterative method, Liszka and McCoy (1982) argued that surface shadowing is a particular multiple-scatter effect. In this solution, each iteration represents an additional surface-to-surface scattering event, either removing previous shadowed rays or adding another surface-to-surface ray to the solution. In numerical studies, however, iterative methods have shown qualified success (Thorsos and Jackson, 1991), and this makes it important to quantify the performance of the HKA before attempting to compensate for its limitations.

B. RFM

In addition to the iterative HIE, there exist a number of exact methods for the periodic surface scattering problem including conformal mappings (Oba, 2010), direct HIE solutions using matrix inversion, and methods based on the Rayleigh hypothesis. The integral equation method is the most relevant exact solution to discussions of the HKA because the two methods share a derivation. The direct HIE solution has been established as a reference for incident plane waves for both rough (Thorsos, 1988) and periodic surfaces (Berman and Perkins, 1990). However, the RFM (Petit et al., 1980, p. 17) was chosen over the HIE for this study because it has a straightforward implementation and efficient solution.

Scattering solution methods based on the Rayleigh hypothesis begin with a periodic surface. For plane wave sources periodic surfaces give rise to Bragg scattering with a finite number of plane wave propagation angles in the far-field. The periodic surface condition may be used to simplify the solution of a number of exact methods, including the HIE (i.e., Abawi, 2011), in terms of these Bragg scattering orders. The Rayleigh hypothesis then assumes further the boundary condition of the problem (in this case a pressure-release boundary) is satisfied on the featured surface by a superposition of out-going plane waves and an evanescent field. For the special case of sinusoidal surfaces with limited slope, the Rayleigh hypothesis has been shown to solve the boundary condition directly (Millar, 1969). The slope limitations for sinusoidal surfaces are sufficient for this study on ocean surface-swell scatter, and the RFM will be considered exact in this discussion.

The RFM reference solution is also useful to determine ranges at which scattering solutions are unnecessary. In many practical experimental setups, a flat-surface reflection model may serve to explain data well. This result has been established for scattering surfaces of all types at the lower limit of grazing angles (Beckmann and Spizzichino, 1987). A number of different source-to-receiver ranges are used to establish when the HKA is accurate, when the image-source is accurate, and when both solutions have significant error. The range where neither solution is appropriate is found to be small, suggesting that with the appropriate choice of model, many transmission scenarios with sinusoidal surfaces can be well modeled by one of these two simple approximations.

C. Model intercomparison

The transmission scenario chosen for this study is a modest extension of wave tank studies by Walstead and Deane (2013). A high-frequency and broadband source signal was used to produce a ray-like transmission scenario for a short source-receiver x-distance, Δx, of 1.2 m (about one surface wavelength). While the surface parameters and acoustic frequencies of this numerical study scale similarly to these studies, a number of separation distances are used to explore the limits of the HKA at low grazing angles. The first part of the model intercomparison studies fixed source and receiver geometry over a complete wave cycle, at a range where the HKA solution begins to show significant error (about five surface wavelengths).

A similar five surface wavelength geometry was also used by Choo et al. (2014) to model scattering observed in channel impulse response measurements taken during sea experiments. In rapidly repeated impulse response measurements, late arriving surface scatter had coherent structure and a change in delay of about 5 ms over a few seconds of measurements (Badiey et al., 2012). This striation pattern was shown by Choo et al. (2014) to arise from eigen-rays interacting with the surface close to the source or receiver. These arrivals have a longer travel distance than eigen-rays interacting with the surface near the flat surface reflection path, and result in large arrivals late in the scattered time series. This study considers a number of source-receiver separations and confirms that these eigen-rays produce a significant contribution to the scattered time series at short ranges, but find they are the largest source of error in the HKA at longer ranges.

A full description of the problem statement and a discussion of the choice of simulation environment is covered in Sec. II. The HKA, ERA, and RFM are covered in detail in Sec. III. The HKA is introduced along with analytical simplifications leading to a time domain solution in Sec. III A. The further analytic approximations leading to the ERA are covered in Sec. III B. The formulation and solution method of the RFM is discussed in Sec. III C. Additionally, Sec. III C covers the wavenumber synthesis required to create

point source results. The scattered time series are computed over the full surface wave cycle at a single range in Sec. IV. The largest difference seen in this comparison is a frequency dependent focusing of the HKA not observed in the RFM, and this effect is explained using ERA. The maximum error between the RFM and HKA solutions is then studied for a number of ranges, and both solutions are compared with flat-surface reflection. Finally, Sec. V summarizes the study.

II. PROBLEM STATEMENT

The three-dimensional setup of the problem along with the coordinate system is shown in Fig. 1. The acoustic point source is located at $\mathbf{r}_{src} = (0, 0, -10\,\text{m})$. The receiver is fixed at a 20-m depth, with a Δx of 200 m. For all simulations the source and receiver are separated exclusively in the x-direction, in-line with the surface wave variation.

The sinusoidal pressure-release surface is defined for wavelength Λ and wave height H as

$$\eta(x, t_{wv}) = \frac{H}{2}\cos\left(\frac{2\pi x}{\Lambda} + \phi(t_{wv})\right). \tag{1}$$

This study fixes the wave parameters to a 2-m wave height and 40-m wavelength. The phase of the surface wave, ϕ, is related to the surface wave time, t_{wv}, by the linear dispersion relationship. The deep-water gravity waves dispersion relationship was used in this study, $\phi(t_{wv}) = t_{wv}\sqrt{2\pi g_0/\Lambda}$, with gravitational acceleration $g_0 = 9.81\,\text{m/s}^2$.

The time variation of the surface wave is solved as a succession of frozen surfaces, assuming that the movement of the ocean surface is much slower than the sound speed in water. Similar to the argument in Walstead and Deane (2013, Appendix A), the short time duration of the transmitted pulse makes it insensitive to the motion of the sea surface. While a full time domain solution is required to quantify this approximation, eigen-rays are used to justify the frozen surface assumption based on two arguments.
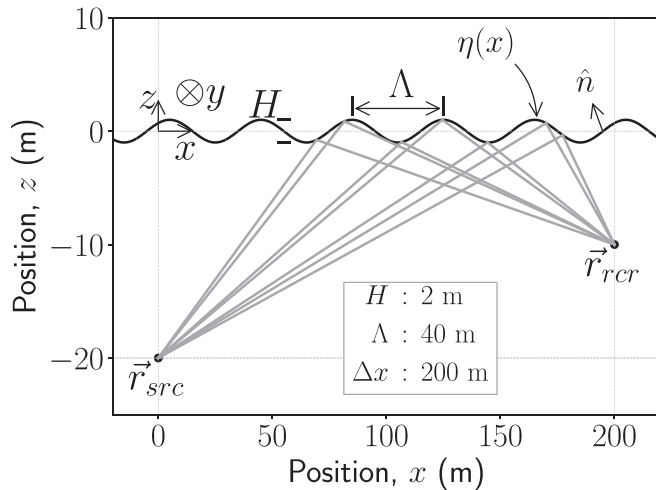

FIG. 1. Basic schematic of the simulation setup used for Figs. 3, 6, and 7. The sinusoidal pressure-release surface has two characteristic length scales, height H and wavelength Λ. A plane view of the surface is drawn, with the y coordinate defined as positive into the page. A radiating half space is assumed as $z \to -\infty$.

First, all eigen-rays interact with the surface within a milli-second of each other, and so all relevant acoustic paths encounter essentially the same wave shape. Second no significant Doppler shift is expected, since for the duration of the acoustic pulse the motion of the surface is a small fraction of the shortest acoustic wavelength.

For a frozen surface and an acoustic time dependence of $\exp(-i2\pi ft)$, the acoustic pressure, $P(x, y, z)$, satisfies the Helmholtz equation

$$(\nabla^2 + k^2)P(x, y, z) = 0. \tag{2}$$

Upper case letters indicate frequency domain functions. The acoustic wavenumber, k, is defined in terms of the acoustic frequency, f, through the dispersion relationship, $k = 2\pi f/c$. The sound speed in the medium, c, is fixed at 1500 m/s.

The total pressure field is split into a sum of two fields, $P(x, y, z) = P_{inc}(x, y, z) + P_{sc}(x, y, z)$. $P_{inc}(x, y, z)$, is the known incident pressure field of an acoustic source in a homogeneous, unbounded medium. $P_{sc}(x, y, z)$, is the unknown scattered pressure field determined by the boundary conditions. The pressure-release boundary condition is

$$-P_{inc}(x, y, \eta(x)) = P_{sc}(x, y, \eta(x)). \tag{3}$$

A radiating boundary condition is required to fully define the problem and can be expressed in general terms (Jensen et al., 2011, p. 79). For incident plane waves, the general radiating condition of the scattered pressure for a homogeneous and otherwise unbounded medium is simplified to an outgoing wave condition (Petit et al., 1980). The outgoing wave condition specifies that, for an incident plane wave, the scattered pressure field below the minimum extent of the surface consists only of plane waves propagating in the $-z$ direction and an exponentially decaying evanescent field.

As shown in Fig. 2, simulation test signals, $s(t)$, are four-cycle sinusoids at three center frequencies: 1.5, 2.5, and 3.5 kHz. A Kaiser-Bessel window with design parameter 2.5 π (α; Kaiser and Schafer, 1980) is applied to reduce side lobes in the frequency domain representation of the signal, $S(f)$. The scattered time series is the real part of the analytic signal given by the one-sided Fourier transform of the signal spectra, $S(f)$, and the pressure field, $P_{sc}(x, y, z, f)$,

$$p_{sc}(x, y, z, t) = 2\text{Re}\left\{\int_0^\infty P_{sc}(x, y, z, f)S(f)\exp(-i2\pi ft)df\right\}. \tag{4}$$

Note that the sign convention adopted here, where positive k values give waves outgoing with time, is opposite that of the discrete Fourier transform.

III. SCATTERING SOLUTION METHODS

The comparison of HKA and RFM solutions in this study are primarily between scattered time series from acoustic point sources. However, the RFM solution exists only for plane wave sources, and both wavenumber and frequency syntheses are required to produce these time series. In contrast, the HKA has a simple integral form for point
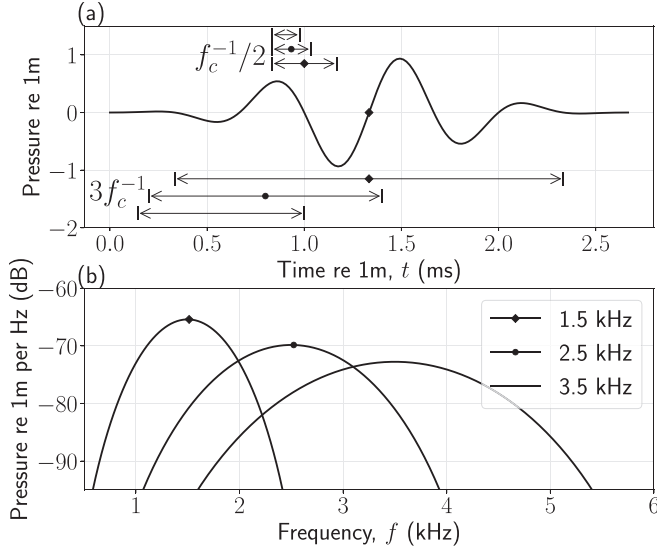
FIG. 2. (a) Time series of 1.5 kHz center frequency transmission, $s(t)$. (b) Fourier transforms of all three transmitted signals, $S(f)$, showing the signals bandwidth are roughly equal to the carrier frequencies: 1.5, 2.5, and 3.5 kHz. All three of the transmitted time series are constructed as four-cycle sinusoids, windowed with a Kaiser-Bessel function, and have the same shape in the time domain. The scaling of the center frequency of the sinusoid has the effect of changing the time scales of the signal, including the half cycle period, $f_c^{-1}/2$, and the duration, defined as $3f_c^{-1}$.

sources (Williams *et al.*, 1994), in addition to a closed-form solution for plane waves (McCammon and McDaniel, 1985). The time domain form of the HKA is derived in Sec. III A. The RFM and the additional wave-number integration required to produce point source results are covered in Sec. III C.

A. HKA

The HKA is an expression for the total pressure field along a boundary in terms of the incident pressure field. This approximation, also known as the local tangent approximation, is equivalent to constructing the scattered field from an integral of infinitesimal flat surface reflections. For a pressure-release boundary, the HKA is

$$\frac{\partial P}{\partial n}(\bar{\mathbf{r}}) \approx 2 \frac{\partial P_{inc}}{\partial n}(\bar{\mathbf{r}}). \qquad (5)$$

An over-bar is used to indicate a position vector along the surface and for each value of (x, y), the z value of the vector $\bar{\mathbf{r}}$ is $\eta(x, y)$. A vector along the surface may be defined alternatively as points at which the function $g(\bar{\mathbf{r}}) = 0$, convenient for surface normal and projected surface area calculations. The definition of $g(x, y, z)$ consistent with the outward surface normal direction, $\hat{n}$ (shown in Fig. 1), is $g(x, y, z) = z - \eta(x, y)$.

The incident field, P_{inc}, is determined using the free-space Green's function. For iso-speed media,

$$G(\mathbf{r}_{src}, \mathbf{r}_{rcr}) = \frac{\exp(ikd_{sr})}{4\pi d_{sr}},$$

$$\nabla G(\mathbf{r}_{src}, \mathbf{r}_{rcr}) \approx ik \frac{(\mathbf{r}_{rcr} - \mathbf{r}_{src})}{d_{sr}} \frac{\exp(ikd_{sr})}{4\pi d_{sr}}, \qquad (6)$$

where $\mathbf{r}_{src}$ and $\mathbf{r}_{rcr}$ are vectors of source location and observation point, respectively, and $d_{sr} = |\mathbf{r}_{rcr} - \mathbf{r}_{src}|$. The far-field approximation was used to simplify the Green's function gradient. The incident normal derivative term of Eq. (5), $\partial P_{inc}(\bar{\mathbf{r}})/\partial n$, is calculated from Eq. (6) using the operator $\partial/\partial n = \hat{n} \cdot \nabla$.

Green's theorem relates the scattered pressure at the receiver to the pressure field at the surface. Excluding the source from the integration volume following Holford (1981), Green's theorem [Jensen *et al.*, 2011, Eq. (2.63)] along the pressure-release surface and the radiating boundary is

$$P_{sc}(\mathbf{r}_{rcr}) = \frac{1}{4\pi} \int\int_{-\infty}^{\infty} \frac{\exp(ik|\mathbf{r}_{rcr} - \bar{\mathbf{r}}|)}{|\mathbf{r}_{rcr} - \bar{\mathbf{r}}|} \Psi(\bar{\mathbf{r}}) dx\, dy, \qquad (7)$$

where the vector $\bar{\mathbf{r}}$ depends on (x, y). The function, $\Psi(\bar{\mathbf{r}})$, is introduced as the product of the normal derivative of the pressure field with the surface differential scaling term, $\Psi(\bar{\mathbf{r}}) = |\nabla g(x, y, \eta)|\, \partial P(x, y, \eta)/\partial n$, projecting the integral onto the $z = 0$ plane.

The HKA is expressed as a two-dimensional integral using the approximation of Eq. (5) in Eq. (7). The resulting integral can be evaluated using numerical quadrature or approximate methods such as stationary phase (e.g., Riley *et al.*, 2006). Either method can be applied to one or both of the integrals. For the flat surface, two applications of the stationary phase approximation to the HKA integral give the exact image-source solution, $-\exp(ikd_{img})(4\pi d_{img})^{-1}$, where d_{img} is the image-source distance.

Following Walstead and Deane (2013), the stationary phase approximation is applied along the y-axis to reduce the surface integral dimension to one. This approximation produces exact results for the surface under study since the y-dimension is an infinite line for each value of x,

$$P_{sc}(\mathbf{r}_r) = \exp(i\,3\pi/4) \sqrt{\frac{k}{2\pi}} \int_{-\infty}^{\infty} \frac{(\bar{\mathbf{r}} - \mathbf{r}_{src}) \cdot \nabla g}{d_{src}}$$
$$\times \frac{\exp[ik(d_{rcr} + d_{src})]}{\sqrt{(d_{rcr} + d_{src})d_{rcr}d_{src}}} dx. \qquad (8)$$

The scalar distances d_{src} and d_{rcr} are $|\bar{\mathbf{r}} - \mathbf{r}_{src}|$ and $|\mathbf{r}_{rcr} - \bar{\mathbf{r}}|$, respectively.

The form of Eq. (8) allows for an analytical evaluation of the Fourier synthesis, Eq. (4), resulting in a time domain equation. With one exception, each of the terms of Eq. (8) depend either on the spatial variable, x, or on the wavenumber, k. After changing the order of spatial and frequency integration, the terms depending on x can be brought outside the Fourier synthesis integration. The only function that has both spatial and wavenumber variables is $\exp[ik(r_{src} + r_{rcr})]$, representing the time shift $\tau(x) = (r_{src} + r_{rcr})/c$. Collecting all complex and frequency dependent terms into the inverse Fourier transform gives the filtered and delayed signal function

$$s_{hk}(t - \tau) = \mathcal{F}^{-1}(\exp(i\,3\pi/4)\sqrt{f}\,S(f)\exp(i\,2\pi f\tau)). \qquad (9)$$

The time domain HKA is then

$$p_{sc}(\mathbf{r}_{rcr}, t) = \sqrt{\frac{1}{c}} \int_{-\infty}^{\infty} \frac{(\bar{\mathbf{r}} - \mathbf{r}_{src}) \cdot \nabla g(x, z)}{d_{src}}$$
$$\times \frac{s_{hk}(t - \tau(x))}{\sqrt{(d_{rcr} + d_{src})d_{rcr}d_{src}}} dx. \qquad (10)$$

B. ERA to the Kirchhoff approximation

The HKA scattering solution can be reduced from an integral to a sum of discrete scattering points using the stationary phase approximation for all integrals in Eq. (7). Barring multiple bounce reflection paths and surface shadowing, the result is equivalent to geometrical acoustics (Williams *et al.*, 1994). Geometric acoustics is a high frequency limit, and expected to give better results with increasing source frequencies. Each term in the stationary phase sum is termed an eigen-ray, and is characterized by a complex amplitude and delay. This approximation then solves for the scattered pressure field as an interference of a few arrivals from different parts of the scattering surface.

The stationary phase approximation is applied to Eq. (8). Collect all non-exponential terms of this equation into the slowly varying function $A(x)$

$$P_{sc}(\mathbf{r}_r) = \exp(i3\pi/4) \sqrt{\frac{f}{c}} \int_{-\infty}^{\infty} A(x)\exp[i\,2\pi f\,\tau(x)]dx. \qquad (11)$$

This leads to the approximate scattering solution

$$P_{sc}(\mathbf{r}_r) = \frac{\exp(i[3\pi/4 \pm \pi/4])}{\sqrt{c}} \sum_n \frac{A(x_n)}{\sqrt{|\tau''(x_n)|}}$$
$$\times \exp\left(i\,2\pi f\,\tau(x_n)\right). \qquad (12)$$

The prime notation, $'$, is used to denote a derivative with respect to x. The sum in Eq. (12) is carried over the n points at which $\tau'(x_n) = 0$. The sign inside the exponential of Eq. (12) is the same as that of $\tau''(x_n)$.

As with the HKA, the Fourier synthesis of the ERA can be evaluated analytically. Two different signals are used in the scattered solution, dependent on the sign of $\tau''(x_n)$. Positive $\tau''(x_n)$ gives a real amplitude term which contributes a delayed and scaled version of the transmitted signal to the scattered result. Negative $\tau''(x_n)$ gives an imaginary amplitude term and contributes a phase shifted version of the transmitted signal,

$$s_-(t - \tau) = -\mathcal{F}^{-1}(i\,S(f)\exp(i\,2\pi f\,\tau)). \qquad (13)$$

A negative sign is included for consistency in a later notation, and this result is the Hilbert transform by standard convention [Oppenheim and Schafer, 2010, Eq. (12.62b)].

Denoting the unmodified transmitted signal as s_+, the scattered pressure field in the time domain is expressed

$$P_{sc}(\mathbf{r}_r) = -\frac{1}{\sqrt{c}} \sum_n \frac{A(x_n)}{\sqrt{|\tau''(x_n)|}} s_\pm(t - \tau(x_n)). \qquad (14)$$

Again, the sign choice for the signal interpolator, $s_\pm(t)$, is the same as that of $\tau''(x_n)$. This sum represents the sum of two convolutions, one for $s_-(t)$ and $s_+(t)$, with a channel represented as a few scaled delta functions.

The ray travel time, $\tau(x)$, and its derivatives are important to determine the amplitude, position, and delay of each eigen-ray. In Fig. 3(b), the total travel time is plotted for the example of the surface wave at $t_{wv} = 0.70$ s. The overall bowl-like shape of $\tau(x)$ is similar to that of the flat surface reflection, with deviations in travel time related to the surface profile. Stationary points appear or disappear from this curve in pairs, preserving the direction of the derivatives at the edges of this curve. The appearance of a pair of stationary points on $\tau(x)$ occurs in three steps: (1) the travel time curve near an edge flattens, (2) two stationary points coincide on the curve, and (3) points are separated in space. The first two steps create eigen-ray shadow and caustic regions, respectively. In eigen-ray shadow regions the stationary phase approximation does not include contributions from a significant region. In eigen-ray caustic regions, $\tau''(x)$ approaches 0 and Eq. (14) grows unbounded.

The interference pattern between multiple eigen-rays means that different source signals have different behaviors for the same channel. For the signal used in this simulation the interference for two rays is largely determined by the center frequency of the signal, f_c, and the spacing of rays less than one period apart, f_c^{-1}. When two signals have the same sign of $\tau''(x_n)$ maximum constructive interference occurs with no delay and maximum destructive interference occurs at half period delay, $f_c^{-1}/2$. For a ray pair, the difference in $\tau''(x_c)$ sign means maximum constructive
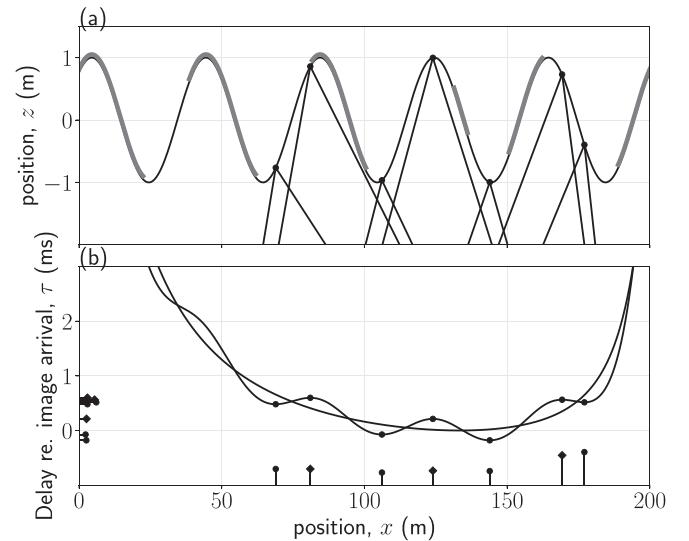

FIG. 3. Simulation setup of Fig. 1, wave at $t_{wv} = 0.70$ s. (a) Spatial position of surface with eigen-rays. Eigen-rays connect the source and receiver and obey specular reflection at the surface (differences in spatial scales may distort perceived angles). Thick patches are shadowed areas of the wave where rays intersect the surface more than once. (b) Travel time, $\tau(x)$, for rays connecting the source and receiver at each point on the surface. Travel time curve for the flat surface is the smooth light line. Relative eigen-ray amplitudes are shown as a function of both position and delay. Rays with circles have real amplitude, while rays with diamonds have imaginary amplitude. The ray pairs closest to the receiver has the largest ray amplitudes, which contribute to a cluster of rays near 0.6 ms delay.

interference occurs at quarter period delay, $f_c^{-1}/4$, and maximum destructive interference at three quarter period delay, $3f_c^{-1}/4$. Away from eigen-ray shadow and caustic regions, the interferences predicted by the ERA agree well with the HKA and explain large peak amplitudes observed in the HKA.

The travel time curve for the wave position of Fig. 1 is shown in Fig. 3. The paths of each eigen-ray, which connect the source and receiver through a specular reflection, are drawn in Fig. 3(a). Each of the extrema of $\tau(x)$ in Fig. 3(b) corresponds to an eigen-ray in Fig. 3(a). In the center of the wave profile eigen-rays appear at the peaks and troughs, while closest to the source and receiver the ray pairs appear on the same wave face. The largest eigen-rays occur in a pair on the wave face closest to the receiver, and these share a delay similar to that of the smaller eigen-ray pair closest to the source. These late arrival features are found consistent in the HKA and ERA solutions for a number of source-receiver x-separations, Sec. IV B.

C. Rayleigh expansion and hypothesis

For an incident plane wave on a periodic surface, the expansion of the scattering solution into a discrete sum of plane and evanescent waves is known as the Rayleigh expansion, represented schematically in Fig. 4. The expansion is the result of the surface periodicity and the plane wave radiation condition. The unknown scattered field is also expressed as the product of an unknown function periodic with scale Λ, and the function $\exp(i\alpha_{inc}x)$ (Petit et al., 1980, p. 9),

$$P_{sc}(x,z) = \exp(i\alpha_{inc}x) \sum_{n=\infty}^{\infty} R_n Z(z) \exp\left(\frac{i2\pi nx}{\Lambda}\right), \quad (15)$$

where the unknowns R_n are the sound pressure *reflection coefficients*. The unknown function, $Z(z,n)$, is determined by Eq. (2) and the outgoing wave condition,

$$Z(z,n) = \exp(-i\gamma_n z), \quad \gamma_n = \sqrt{k^2 - \left(\alpha_{inc} + \frac{2\pi n}{\Lambda}\right)^2}. \quad (16)$$
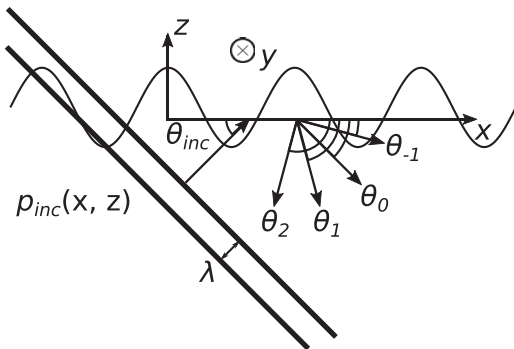

FIG. 4. Schematic of the Rayleigh expansion. An incident plane wave propagates with angle θ_{inc} toward the pressure-release surface. Two lines of constant phase are shown with a one acoustic wavelength, λ, spacing. The incident field does not interact with the surface, and the constant phase lines are drawn through the surface as though it were not there. The Bragg scattering angles are numbered, where θ_0 is the specular reflection angle when $\cos(\theta_{inc}) = \cos(\theta_0)$.

The Rayleigh hypothesis then makes the assumption that the Rayleigh expansion converges to the true pressure field at the pressure-release surface itself (Millar, 1973). This hypothesis holds for sinusoidal scattering surfaces with maximum slope ($\pi H/\Lambda$) of 0.448 or less (Millar, 1969), but not for general periodic surfaces. When this hypothesis holds, the scattering problem is simplified to finding the complex amplitudes of a number of outgoing plane waves. This study uses the RFM to solve for these unknown amplitudes, leading to an infinite system of equations relating to Fourier series coefficients. The Galerkin method is used to solve this infinite system of equations, simply truncating it after a few evanescent orders. The reflection coefficients from this method conserved energy beyond 99.9% [Eq. 9 in Holford, 1981] for all calculated values, and are considered exact.

Each term in Eq. (15) represents a plane or evanescent wave with horizontal wavenumber $\alpha_n = \alpha_{inc} + 2\pi n/\Lambda$, and vertical wavenumber, γ_n. The propagation directions of these plane waves are the Bragg angles (Petit et al., 1980, p.11),

$$\cos(\theta_n) = \cos(\theta_{inc}) + n\frac{\lambda}{\Lambda}. \quad (17)$$

Each term with $|\cos(\theta_{inc}) + n\lambda/\Lambda| < 1$ is a plane wave propagating away from the surface, and otherwise is an evanescent wave decaying exponentially as $z \to -\infty$.

The RFM uses the expansion of Eq. (15) directly in the boundary condition of Eq. (3). The resulting equality between two periodic functions is solved as an equality between Fourier coefficients. For the sinusoidal surface of Eq. (1), the Fourier coefficients are analytic, and the RFM gives

$$-i^m J_m\left(\gamma_{inc}\frac{H}{2}\right) = \sum_{n=-\infty}^{\infty} i^{n-m} R_n J_{n-m}\left(-\gamma_n \frac{H}{2}\right), \quad (18)$$

where J_m is a Bessel function of the first kind with order m. This infinite system of equations is solved by truncation after a finite number of terms. Three positive and three negative evanescent orders of n were found sufficient for energy conservation, while including too large a number of evanescent orders introduced numerical instability.

For comparison with RFM calculations, the reflection coefficients of the HKA have a closed form (McCammon and McDaniel, 1985),

$$R_n = i^n \frac{\alpha_{inc}(\alpha_n - \alpha_{inc}) - \gamma_{inc}(\gamma_{inc} + \gamma_n)}{\gamma_n(\gamma_{inc} + \gamma_n)}$$
$$\times J_n\big((\gamma_{inc} + \gamma_n)H/2\big). \quad (19)$$

The phase term, i^n, was added to this expression following McCammon (1984), and gives $R_0 = -1$ when $H = 0$.

The HKA and RFM reflection coefficients are shown at 500 Hz in Fig. 5. This low frequency was chosen for ease of visualization because it has the least variation with θ_{inc}, but the behavior comparison is similar at higher frequencies. The surface profile is symmetric about $x = 0$, requiring $R_n(\theta_{inc}) = R_{-n}(180° - \theta_{inc})$. The HKA coefficients are indistinguishable from the RFM for θ_{inc} between 40° and
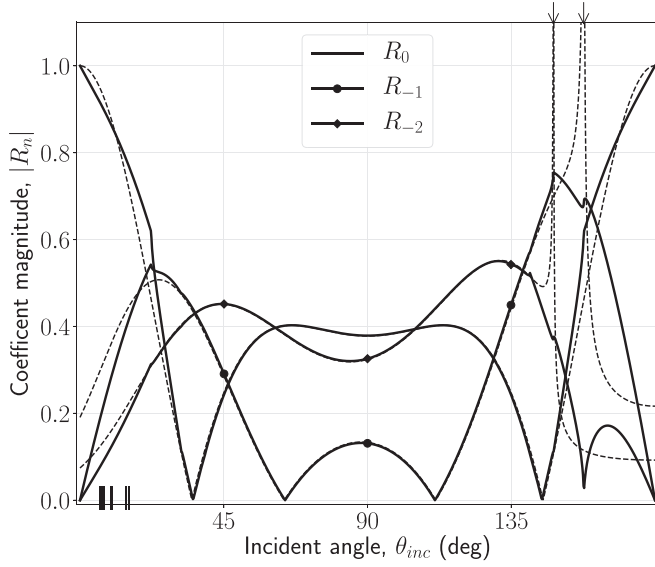
FIG. 5. Magnitude of the reflection coefficients, $R_n(\alpha_{inc})$, computed using RFM and HKA at 500 Hz for a sinusoidal surface with a 2-m wave height and a 40-m wavelength. The RFM results are plotted as solid lines, while the HKA is plotted as lighter dashed lines. For symmetric surface profiles, the reflection coefficients of order n are the same as that for order $-n$, mirrored about $\theta_{inc} = 90°$. The angles at which each Bragg order become evanescent are marked on top of the graph with arrows, and the HKA coefficients grow unbounded at these angles. The incident angles of the eigen-rays for the experimental setup of Fig. 1 at $t_{wv} = 0.70$ s are plotted as ticks along the bottom axis.

140°, covering near-vertical incidence. All of the eigen-ray angles for the test scenario of Fig. 1 are less than 20°, and are indicated as ticks along the θ_{inc} axis in Fig. 5. For negative Bragg orders, these angles are past where the two solution methods diverge, below $\theta_{inc} = 40°$. The largest discrepancy between the RFM and the HKA solutions is largest at the cutoff angle for each Bragg order (31.7° and 22.3° for orders 2 and 1), where the HKA predicts unbounded amplitude, while the RFM remains bounded.

A wavenumber synthesis is required to produce point source scattering from the plane wave results of the RFM

$$P_{sc}(\mathbf{r}) = \frac{i}{8\pi^2} \sum_{n=-\infty}^{\infty} \iint_{-\infty}^{\infty} R_n(\alpha_{inc}, \beta)$$

$$\times \frac{\exp\left(i \left(\begin{bmatrix} \alpha_n \\ \beta \\ -\gamma_n \end{bmatrix} \cdot \mathbf{r}_{rcr} - \begin{bmatrix} \alpha_{inc} \\ \beta \\ \gamma_{inc} \end{bmatrix} \cdot \mathbf{r}_{src} \right) \right)}{\gamma_{inc}}$$

$$\times \, d\alpha_{inc} \, d\beta. \tag{20}$$

The horizontal wavenumber in the y-dimension is introduced as β, with the requirement $k^2 = \alpha^2 + \beta^2 + \gamma^2$. Holford (1981) noted that for y-independent surfaces, the solution for $R_n(\alpha_{inc}, \beta)$ at all β can be constructed from the plane wave with $\beta = 0$ and a modified value of $k_{2d}^2 = k^2 - \beta^2$.

The stationary phase approximation in α_{inc} and β is used to compute point source results from Eq. (20). The phase function of the wavenumber integral is simple, with a single stationary point for each term in Eq. (20). For source and receivers at $y = 0$, the stationary phase approximation is

$$P_{sc}(\mathbf{r}) \approx \sum_{n=-\infty}^{\infty} R(\alpha_{inc}) \frac{\exp[i(\alpha_n x_r - \alpha_{inc} x_s - \gamma_n z_r + \gamma_{inc} z_s)]}{4\pi k \gamma_{inc}}$$

$$\times \left(\left| \frac{z_r}{\gamma_{inc}^3} + \frac{z_s}{\gamma_n^3} \right| \left| \frac{z_r}{\gamma_{inc}} + \frac{z_s}{\gamma_n} \right| \right)^{-1/2}. \tag{21}$$

This function is evaluated at stationary points when $x_s = x_r + \alpha_n z_r / \gamma_n + \alpha_{inc} \, z_s / \gamma_{inc}$. The errors associated with the stationary phase approximation are related to the rapidly changing values of $R_n(\alpha_{inc})$, evident in Fig. 5. These errors were found to be small by comparing synthesized HKA results using Eqs. (19) and (21) with time series solutions computed using Eq. (10).

IV. RESULTS

Time series transmissions are compared between the HKA of Eq. (10), the ERA of Eq. (14), and the RFM constructed with the wavenumber and time synthesis of Eqs. (21) and (4). To highlight the effect of the featured surface, the amplitudes in the following plots are divided by the amplitude of the image arrival, $(4\pi r_{img})^{-1}$, and the image delay, r_{img}/c, is subtracted from the acoustic time scale, t. In Sec. IV A Δx is fixed at 200 m. The surface wave position is allowed to vary as a function of wave time, t_{wv}, according to Eq. (1). In Sec. IV B, Δx is varied between 50 and 1000 m. A single wave position is chosen for each range which produces the largest peak arrival in the HKA results. The remaining simulation parameters are constant, as discussed in Sec. II and plotted in Fig. 1.

A. Full surface wave cycle simulations

The 2.5 kHz signal scattered time series is presented as color-maps in Fig. 6 over the full surface wave cycle for $\Delta x = 200$ m. There is good agreement between the HKA and RFM in the time dilation of the pulse, the distribution of energy through the scattered arrival, and the location of major focusing events. The ERA and the HKA are in agreement up until the caustic region, apparent in the ERA as a sharp increase in amplitude followed by the sudden disappearance of acoustic pressure. In contrast, the HKA predicts a smooth decrease of acoustic pressure through this region.

The largest discrepancy between HKA and RFM is in the amplitudes of the largest peak pressure, around surface wave time, t_{wv}, of 0.70 s (indicated by a vertical line in Fig. 6). These scattering results are shown in Fig. 7 for three acoustic center frequencies: (a) 3.5, (b) 2.5, and (c) 1.5 kHz. There are no significant eigen-ray shadow or caustic regions near the receiver, and ERA does well in predicting the HKA result. For the higher source frequencies shown in Figs. 7(a) and 7(b), the rays that make up the scattered time series are separated in time, with low amplitude arrivals before 1 ms, and higher amplitude arrivals after 1 ms delay. This structure is not apparent in Fig. 7(c), where the longer time width of the 1.5 kHz signal merges the eigen-ray arrivals. For all frequencies, this surface wave position leads to focusing and the late arrival amplitudes exceed the image arrival (i.e., >1).

While the HKA over-estimates the signal amplitude for almost the entire time series for each frequency, the most

J. Acoust. Soc. Am. **144** (3), September 2018
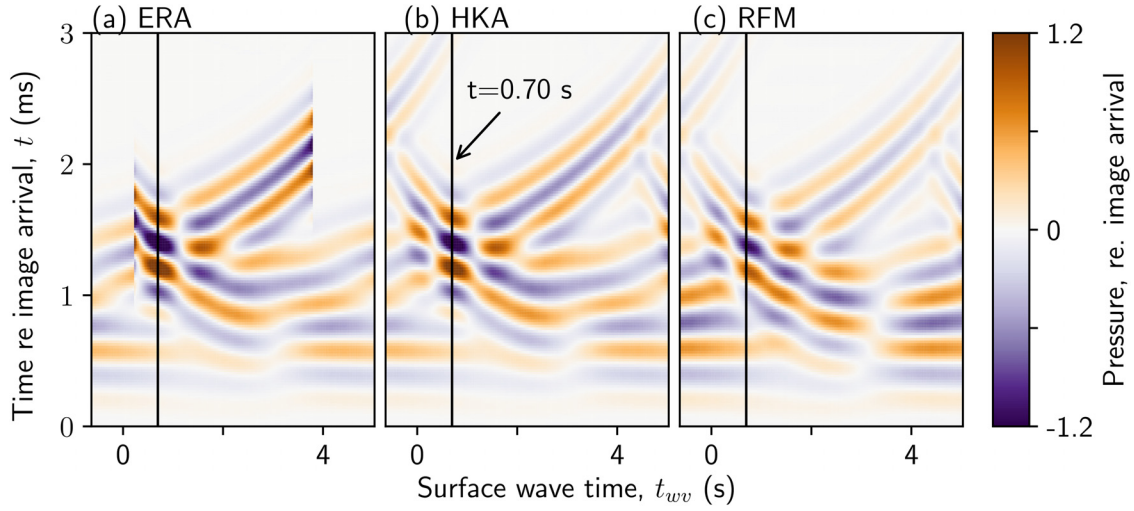
Richards *et al.*   1275

FIG. 6. (Color online) Scattered time series plotted over a single surface wave period for 2.5 kHz center frequency pulse and simulation setup of Fig. 1: (a) ERA, (b) HKA, and (c) RFM results. The scattered pressure, $p_{sc}(t)$, is plotted referenced to the image (flat surface) arrival.

significant disagreement between the solutions is for the peak pressures at the middle probe signal frequency [2.5 kHz; Fig. 7(b) around 1.5 ms]. The eigen-ray arrival structure for 200-m Δx, shown in Fig. 8(a), produces an ERA result similar to the HKA. The large amplitude eigen-ray arrivals around 0.6 ms delay are most relevant for determining the peak pressure. This ray pair is close to the optimal constructive spacing of 1/10 ms for the 2.5 kHz center frequency signal, and the total interference result produces the largest peak pressures for this signal. The reference RFM solution, however, does not show the large peak pressures observed for the 2.5 kHz signal by the HKA. This over-

prediction of the late arrivals is further demonstrated as Δx is increased and the differences between the RFM and HKA become marked.

B. Multiple source-receiver separations

To study the effect of lower surface grazing angles Δx was incremented in 50-m range steps from 50 to 1000 m. The surface wave position resulting in the largest peak HKA arrival was identified for inter-range comparison. These HKA and RFM time series are presented in Fig. 9. The eigen-rays for this wave position are shown in Fig. 8(b). The delay of the largest HKA arrivals is highlighted by a gray box for both solutions, and this corresponds to the delay highlighted in Fig. 8 after convolution with the source signal. The basic shape of the HKA result, Fig. 9(b), remains
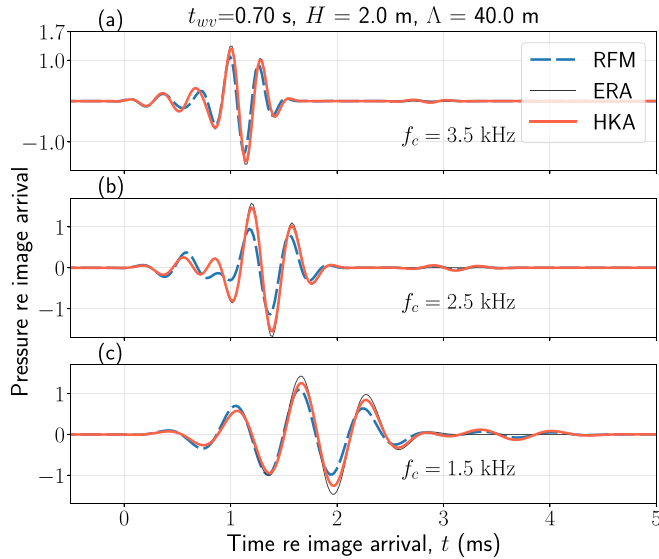

FIG. 7. (Color online) Scattered time series for surface wave phase at $t_{wv} = 0.70$ s, using the simulation setup shown in Fig. 1. Each panel shows results for one of three source center frequencies, f_c, computed using RFM, the HKA, and the ERA: (a) 3.5, (b) 2.5, and (c) 1.5 kHz. The shape of the time series is similar between the RFM and HKA solution methods, though the HKA consistently over-predicts the largest amplitudes at each center frequency. The HKA over-prediction is greatest for the 2.5-kHz transmission between 1 and 1.5 ms. The ERA agrees well with the HKA, with a slight over-prediction, largest at 1.5 kHz.
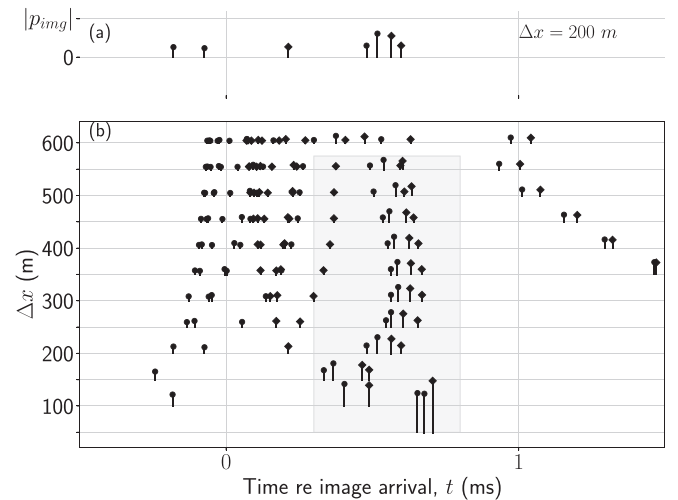

FIG. 8. Eigen-ray delay and amplitude, normalized to image arrival, for the wave position creating the largest HKA peak amplitude. Rays with circles have real amplitude, while rays with diamonds have imaginary amplitude. (a) The rays for the test setup of Fig. 1. (b) Shows rays making up the largest HKA peak arrival at 50-m increments of source-receiver separation. The approximate delay times of the largest arrivals are highlighted in gray for ranges with strong late arrival rays.
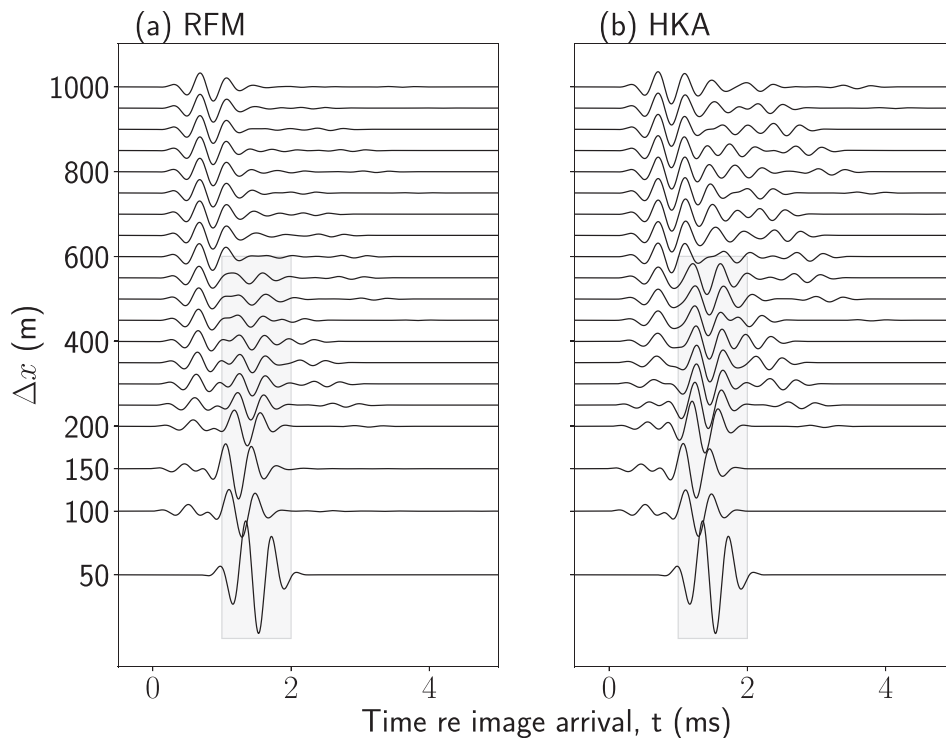
FIG. 9. Cascade plot of acoustic pressure time series at wave time producing the largest arrival in the HKA solution for $f_c = 2.5\,\text{kHz}$. Δx is increased by 50 m for each acoustic time series, while all other simulation parameters are the same as in Fig. 1: (a) RFM solution and (b) HKA solution. The delay times of the largest HKA arrivals are highlighted in gray for ranges where this is clearly associated with late arrival rays. The acoustic time series is first normalized in amplitude and delay to the image arrival, and then scaled by 40 for legibility. The vertical spacing for the 50, 100, and 150 m time series have been increased to improve legibility, while the rest of the time series have a constant offset of 50 m.

consistent as Δx is varied from 200 m, with large late arrivals occurring up to 600-m Δx. The HKA time spread for the 2.5 kHz signal remains larger than 2 ms for all ranges, sometimes up to 4 ms. This is consistent with the late eigen-rays around 0.6 ms, Fig. 8(b), which reflect close to the receiver and show large amplitudes for all ranges up to 600 m. Additionally, for Δx beyond 350-m, very late eigen-rays with about 1.5 ms delays are apparent which reflect from the surface near the source. The majority of the eigen-rays, occurring in the middle of the travel time curve, approach the flat surface travel time curve as the range increases and interferes to create an image source at long ranges.

The RFM solution in Fig. 9(a) agrees well with the HKA up to Δx of 200 m, when distinctions become apparent. The late arrivals fade with increasing Δx past 200-m and are hardly significant beyond 400 m. Additionally, eigen-rays with delays of more than 1.5 ms do not appear significant in the RFM solution. Finally, beyond 600-m Δx the RFM is virtually indistinguishable from the image solution, while the HKA only approaches this result around 1000-m Δx. This result is consistent with the reflection coefficients in Fig. 5 which shows the 0th RFM coefficient approaches 1 the angle of incidence approaches $0°$, while other coefficients approach 0. The 0th HKA coefficient also approaches 1 as the angle of incidence approaches $0°$, but the negative Bragg orders approach non-zero values. The eigen-rays of Fig. 8 and the time series of Fig. 9 demonstrate that the HKA error seen in reflection coefficients at low grazing angles is the result of late arrival rays. These rays, reflecting from the surface near the source and receiver, are well modeled by the HKA for small Δx values, but become the dominant source of error for larger Δx values.

The error of the HKA compared to the RFM and the image solution is shown against range in Fig. 10. This error

is calculated as the integral in time, t, of the absolute difference between two solutions for a fixed surface wave position. This result is then normalized by the image-source amplitude to remove the effect of spreading loss. There is little mismatch between the RFM and the HKA for Δx values up until 150 m. The error between the two solutions begins to increase sharply at this point, and the difference between the two solutions levels off around 300 m Δx. At 350-m and greater Δx, the simple image-source solution has a less integrated absolute difference compared to the RFM. This suggests the image solution is preferred over the HKA at 350 m and beyond for the test scenario under consideration.
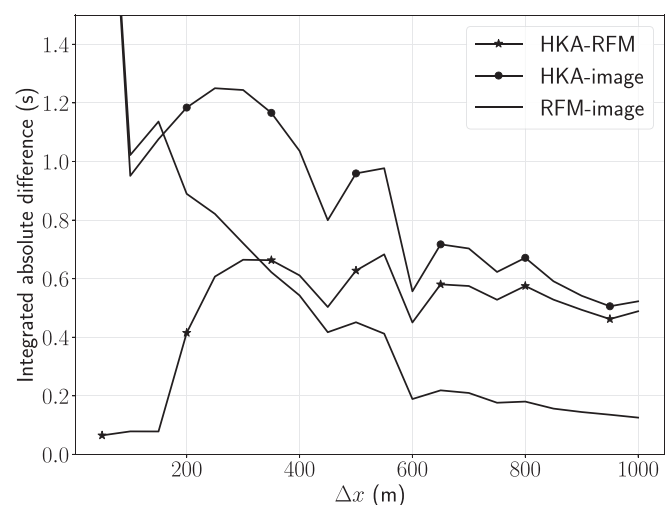

FIG. 10. Absolute difference of acoustic pressure integrated over time (t) at the surface wave time (t_{wv}) of maximum HKA arrival. Comparisons are taken between: RFM and HKA, HKA and image-source, and RFM and image-source. For each range, the RFM and HKA time series used in the integration are the same as those plotted in Fig. 9.

V. SUMMARY

For sinusoidal surfaces (40-m wavelength, 20-m source, and 10-m receiver depths) at short Δx (up to 150-m), HKA results agreed with reference RFM solutions. At moderate Δx (around 200 m), the HKA sometimes over-estimated the peak pressure, dependent on the frequency of the signal tested. Eigen-ray interferences were used as an explanation for the frequency dependent HKA over-prediction. As the source-receiver x-separation was extended to longer ranges (past 200 m), the error of the HKA increased significantly at all frequencies. The HKA continued to predict large amplitude late arrival features up to 550-m Δx and significant acoustic time spread up to 1000-m Δx. In contrast, the RFM approached the image-source solution quickly for Δx past 350 m. After 350-m Δx the image-source approximation had a less integrated mismatch with the reference RFM than the HKA.

This study used the RFM reference solution to inform the application of the more practical and flexible HKA. As Δx was extended to explore low grazing angles the HKA began to show a significant error. The range for which the HKA is a useful approximation extended for some distance past the point suggested by plane wave reflection coefficients. When solving for acoustic scatter from monochromatic surface waves at short ranges, the HKA was found to be a useful method for modeling and understanding acoustic scatter in the time domain. The monochromatic surface solution modeled by the RFM is expected to give relevant bounds on experimental geometries for which the HKA result is accurate, and lend credence when using the approximation for more complicated scattering problems with the same geometries.

ACKNOWLEDGMENTS

Abawi, A. T. (**2011**). "The use of the virtual source technique in computing scattering from periodic ocean surfaces," J. Acoust. Soc. Am. **130**(2), 683–688.

Badiey, M., Song, A., and Smith, K. B. (**2012**). "Coherent reflection from surface gravity water waves during reciprocal acoustic transmissions," J. Acoust. Soc. Am. **132**(4), EL290–EL295.

Beckmann, P., and Spizzichino, A. (**1987**). *The Scattering of Electromagnetic Waves From Rough Surfaces* (Artech House, Inc., Norwood, MA), 511 p.

Berman, D. H., and Perkins, J. S. (**1990**). "Rayleigh method for scattering from random and deterministic interfaces," J. Acoust. Soc. Am. **88**(2), 1032–1044.

Choo, Y., Seong, W., and Song, H. (**2014**). "Emergence of striation patterns in acoustic signals reflected from dynamic surface waves," J. Acoust. Soc. Am. **136**(3), 1046–1053.

Choo, Y., Song, H. C., and Seong, W. (**2016**). "Numerical study of three-dimensional sound reflection from corrugated surface waves," J. Acoust. Soc. Am. **140**(4), 2290–2296.

Choo, Y., Song, H. C., and Seong, W. (**2017**). "Time-domain Helmholtz-Kirchhoff integral for surface scattering in a refractive medium," J. Acoust. Soc. Am. **141**(3), EL267–EL273.

Holford, R. (**1981**). "Scattering of sound waves at a periodic, pressure-release surface: An exact solution," J. Acoust. Soc. Am. **70**(4), 1116–1128.

Jensen, F., Kuperman, W., Porter, M., and Schmidt, H. (**2011**). *Computational Ocean Acoustics* (Springer, New York).

Kaiser, J., and Schafer, R. (**1980**). "On the use of the I0-sinh window for spectrum analysis," IEEE Trans. Acoust., Speech, Signal Process. **28**(1), 105–107.

Keiffer, R. S., and Novarini, J. C. (**2000**). "A time domain rough surface scattering model based on wedge diffraction: Application to low-frequency backscattering from two-dimensional sea surfaces," J. Acoust. Soc. Am. **107**(1), 27–39.

Liszka, E., and McCoy, J. (**1982**). "Scattering at a rough boundary—Extensions of the Kirchhoff approximation," J. Acoust. Soc. Am. **71**(5), 1093–1100.

McCammon, D. F. (**1984**). "An evaluation of the Kirchhoff approximation for acoustic plane wave reflection coefficients from a sinusoidal boundary," Ph.D. thesis, The Pennsylvania State University.

McCammon, D. F., and McDaniel, S. T. (**1985**). "Application of a new theoretical treatment to an old problem; Sinusoidal pressure release boundary scattering," J. Acoust. Soc. Am. **78**(1), 149–156.

Meecham, W. C. (**1956**). "On the use of the Kirchhoff approximation for the solution of reflection problems," J. Rational Mech. Anal. **5**(2), 323–334.

Millar, R. F. (**1969**). "On the Rayleigh assumption in scattering by a periodic surface," Math. Proc. Cambridge Philos. Soc. **65**(3), 773–791.

Millar, R. F. (**1973**). "The Rayleigh hypothesis and a related least-squares solution to scattering problems for periodic surfaces and other scatterers," Radio Sci. **8**(8–9), 785–796, https://doi.org/10.1029/RS008i008p00785.

Oba, R. M. (**2010**). "Global boundary flattening transforms for acoustic propagation under rough sea surfaces," J. Acoust. Soc. Am. **128**(1), 39–49.

Oppenheim, A., and Schafer, R. (**2010**). *Discrete-Time Signal Processing* (Pearson Education, Upper Saddle River, NJ).

Petit, R., Botten, L., Cadilhac, M., Derrick, G., Maystre, D., McPhedran, R., Neviere, M., and Vincent, P. (**1980**). "Topics in current physics," in *Electromagnetic Theory of Gratings* (Springer, Berlin Heidelberg).

Riley, K., Hobson, M., and Bence, S. (**2006**). *Mathematical Methods for Physics and Engineering: A Comprehensive Guide* (Cambridge University Press, Cambridge).

Senne, J., Song, A., Badiey, M., and Smith, K. B. (**2012**). "Parabolic equation modeling of high frequency acoustic transmission with an evolving sea surface," J. Acoust. Soc. Am. **132**(3), 1311–1318.

Thorsos, E. I. (**1988**). "The validity of the Kirchhoff approximation for rough surface scattering using a Gaussian roughness spectrum," J. Acoust. Soc. Am. **83**(1), 78–92.

Thorsos, E. I., and Broschat, S. L. (**1995**). "An investigation of the small slope approximation for scattering from rough surfaces. Part I. Theory," J. Acoust. Soc. Am. **97**(4), 2082–2093.

Thorsos, E. I., and Jackson, D. R. (**1991**). "Studies of scattering theory using numerical methods," Waves Random Media **1**(3), S165–S190.

Walstead, S. P., and Deane, G. B. (**2013**). "Reconstructing surface wave profiles from reflected acoustic pulses," J. Acoust. Soc. Am. **133**(5), 2597–2611.

Walstead, S. P., and Deane, G. B. (**2016**). "Intensity statistics of very high frequency sound scattered from wind-driven waves," J. Acoust. Soc. Am. **139**(5), 2784–2796.

Williams, K., Stroud, J., and Marston, P. (**1994**). "High-frequency forward scattering from Gaussian spectrum, pressure release, corrugated surfaces. I. Catastrophe theory modeling," J. Acoust. Soc. Am. **96**(3), 1687–1702.